scientific reports

OPEN

Ab initio study of mechanical and thermal properties of GeTe-based and PbSe-based high-entropy chalcogenides

Sahib Hasan[1,2], Puja Adhikari[1], Saro San[1] & Wai-Yim Ching[1✉]

GeTe-based and PbSe-based high-entropy compounds have outstanding thermoelectric (TE) performance and crucial applications in mid and high temperatures. Recently, the optimization of TE performance of high-entropy compounds has been focused on reducing thermal conductivity by strengthening the phonon scattering process to improve TE performance. We report a first-principles investigation on nine GeTe-based high-entropy chalcogenide solid solutions constituted of eight metallic elements (Ag, Pb, Sb, Bi, Cu, Cd, Mn, and Sn) and 13 PbSe-based high-entropy chalcogenide solid solutions: $Pb_{0.99-y}Sb_{0.012}Sn_ySe_{1-2x}Te_xS_x$ (x = 0.1, 0.2, 0.25, 0.3, 0.35, 0.4, 0.45, and y = 0) and $Pb_{0.99-y}Sb_{0.012}Sn_ySe_{1-2x}Te_xS_x$ (y = 0.05, 0.1, 0.15, 0.2, 0.25 and x = 0.25). We have investigated the mechanical properties focusing on Debye temperature (Θ_D), thermal conductivity (κ), Grüneisen parameter (γ_α), dominant phonon wavelength (λ_{dom}), and melting temperature (T_m). We find that the lattice thermal conductivity is significantly reduced when GeTe is alloyed into the following compositions: $Ge_{0.75}Sb_{0.13}Pb_{0.12}Te$, $Ge_{0.61}Ag_{0.11}Sb_{0.13}Pb_{0.12}Bi_{0.01}Te$, and $Ge_{0.61}Ag_{0.11}Sb_{0.13}Pb_{0.12}Mn_{0.05}Bi_{0.01}Te$. This reduction is due to the mass increase and strain fluctuations. The results also show that $Ge_{0.61}Ag_{0.11}Sb_{0.13}Pb_{0.12}Bi_{0.01}Te$ solid solution has the lowest Young's modulus (30.362 GPa), bulk and shear moduli (18.626 and 12.359 GPa), average sound velocity (1653.128 m/sec), Debye temperature (151.689 K), lattice thermal conductivity (0.574 $W.m^{-1}.K^{-1}$), dominant phonon wavelength (0.692 Å), and melting temperature (535.91 K). Moreover, $Ge_{0.61}Ag_{0.11}Sb_{0.13}Pb_{0.12}Bi_{0.01}Te$ has the highest Grüneisen parameter with a reduced and temperature-independent lattice thermal conductivity. The positive correlation between Θ_D and κ is revealed. Alloying of PbSe-based high-entropy by Sb, Sn, Te, and S atoms at the Se and Pb sites resulted in much higher shear strains resulted in the reduction of phonon velocity, a reduced Θ_D, and a lower lattice thermal conductivity.

High-entropy alloys (HEAs) are alloys with high configuration entropy obtained by increasing the number of constituting elements (n) with $n \geq 5$[1]. The atomic concentration of elements in high-entropy (HE) materials can be between 5 and 35% of the samples[2,3]. The concept of HE originated from the hypothesis that the solid solution is stabilized by a high configurational entropy of mixing[4]. Alternative criterion to define a HE material is the value of entropy of mixing ΔS_{mix} expressed as $\Delta S_{mix} = -R \sum_{i=1}^{N} x_i ln x_i$, where R, N, and x_i are the gas constant, number of components, and atomic fraction of the components, respectively[5]. Materials can be classified as low-entropy (ΔS_{mix} less than 0.69R), medium-entropy (ΔS_{mix} between 0.69R and 1.59R) and high-entropy (ΔS_{mix} larger than 1.60R)[6]. The synthesis of HE materials is an emerging field of research which aims to design multicomponent single-phase materials. The multicomponent materials contain a minimum of 5 elements in nearly equal atomic ratios or not so equal in high-entropy metal alloys (HEMAs). HEMAs have a wide range of remarkable mechanical[7,8], dielectric[9], and superconducting[10] properties. Recently, researchers found that HE materials can be disordered with severe lattice distortions and non-diffusion characteristic of the atoms contained therein exhibiting low thermal stability[11]. The scattering of phonons increases due to the severe lattice distortion, thus reducing lattice thermal conductivity of HE materials[12]. Single phase HEAs possess high hardness[13], high

[1]Department of Physics and Astronomy, University of Missouri-Kansas City, Kansas City, MO 64110, USA. [2]Department of Sciences, College of Basic Education, Al Muthanna University, Samawah 66001, Iraq. ✉email: chingw@umkc.edu

strength[14], good wear[15], and erosion resistance[16]. Other multicomponent compounds, such as high-entropy oxides (HEOs)[17, 18], borides[19], and carbides[20, 21] have also been synthesized recently.

Despite the intense research on HE materials, HE materials with semiconducting characteristics have not yet been explored. HE materials having a band gap have a wide range of electronic, thermoelectric, and optical applications[22–24]. The alloying of semiconductors has been employed to enhance the electronic, structural, and other functional characteristics, resulting in many emergent properties. For example, some alloyed semiconductors such as chalcogenides exhibit low thermal conductivity, tunable optical emission, and higher number of carrier mobility[25–28]. Chalcogenides with semiconducting characteristics contain at least one of the elements: tellurium (Te), selenium (Se), and sulfur (S). In particular, the family of IV – VI compounds have attracted a great attention due to their optoelectronic, microelectronic, and high thermoelectric (TE) performance[29, 30]. Recently, the most investigated category of IV – VI semiconductor chalcogenides are: SnS[31], SnSe[32], SnTe[33], GeSe[34], GeTe[35], PbS[36], PbSe[37] and PbTe[38].

The direct conversion of heat into electricity under a temperature gradient is carried out by thermoelectric (TE) devices. TE technology is one of the promising green solutions to mitigate the energy and environment crisis[39]. The performance of TE devices is described by the parameter ZT called figure of merit defined as $ZT = S^2\sigma T/\kappa$, where σ is the electrical conductivity, S is the Seebeck coefficient, T is the absolute temperature, and κ is the thermal conductivity. To improve the TE performance of chalcogenides, doping and alloying have been applied recently. For example, TE performance of $Bi_2(Te,Se)_3$, $Sn(S,Se)$, and GeTe alloys has shown to be enhanced[40–44]. The attempts to improve TE performance, by increasing TE power factor (PF) and lowering the lattice thermal conductivity (κ_L) have skyrocketed. Other attempts include introducing the configurational entropy via doping or alloying techniques[45]. For examples, chalcogenide compounds $Ge_{0.84}In_{0.01}Pb_{0.1}Sb_{0.05}Te_{0.997}I_{0.003}$[29], $PbSnTeSe$[46], and $(Sn_{0.7}Ge_{0.2}Pb_{0.1})_{0.75}Mn_{0.275}Te$[47] achieved the enhancement of TE performance. Apparently, this strategy has been successful[48]. The sluggish diffusion and sever lattice distortion[49] in HE materials have induced many fascinating TE properties such as low κ_L and very high ZT[50, 51]. HEA are widely used to enhance TE performance in many chalcogenide systems such as $(SnGePbMn)Te$[47], $BiSbTe_{1.5}Se_{1.5}$[52], and $(PbTe)_{1-2x}(PbSe)_x(PbS)_x$[53]. A high figure of merit ($ZT = 1.42$ at 900 K) was achieved[47] in $(Sn_{0.74}Ge_{0.2}Pb_{0.1})_{0.75}Mn_{0.275}Te$.

Among chalcogenide materials, germanium telluride GeTe[54] is a promising semiconductor with a narrow band gap and good TE performance. GeTe belongs to the IV-VI group and has rhombohedral crystal structure ($R3m$) at room temperature[55, 56]. It exhibits a sudden phase transition to the cubic rock-salt structure (Fm-3 m) at around 700 K[57]. Compared to PbTe and SnTe, GeTe is much less explored. Pure GeTe has average TE properties with maximum ZT of less than 0.8 at 720 K[58]. Electronic structure, dynamical, dielectric, and elastic properties of pure GeTe was investigated using density functional perturbation theory by R. Shaltaf et al.[59]. They used the Hartwigsen-Goedecker-Hutter pseudopotentials including spin–orbit coupling to achieve high accuracy of the calculations. They found that GeTe is a semiconductor with a direct energy band gap of 0.48 eV. However, alloyed and doped rhombohedral crystals of GeTe with high TE performance have been reported[60, 61] revealing its reduced lattice thermal conductivity and higher ZT ($ZT \approx 2.2$). This was achieved in $Ge_{1-x-y}Sb_xIn_yTe$[62], $Ge_{1-x-y}Sb_x Zn_yTe$[63], and $Ge_{1-x-y}Bi_xCd_yTe$[64]. Other attempts were carried out to reduce the phase transition temperature of GeTe by dual-doping of Sb and Mn[57], and Bi and Mn[65]. Thus, TE performance of alloyed and doped GeTe was enhanced in the medium temperature range of 700 K. By introducing Ag, Sb, Pb, and Bi to Ge sites to form a high-entropy GeTe-based material, higher electrical transport and lower thermal conductivity were achieved by Jiang et al.[66].

Lead chalcogenides PbX (X = S, Se and Te) have been extensively studied in the last decades due to their applications as TE materials available at medium temperature (400–900 K)[67–70]. They belong to the IV-VI group and have a simple NaCl-type (B1) structure at ambient conditions. They are narrow gap semiconductors having low thermal conductivities even at high temperatures (500–700 k)[71]. This makes them good TE materials. TE performance of PbSe was enhanced by doping with elements such as B, Ga, In, Tl, Pb[72, 73], Al[74], Sb[75], and Bi[76]. HE technique has also been used to achieve high TE performance of PbSe-based HE compounds. Jiang et al. studied TE performance of $Pb_{0.89}Sb_{0.012}Sn_{0.1}Se_{0.5}Te_{0.25}S_{0.25}$[77], $Pb_{0.975}Na_{0.025}Se_{0.5}S_{0.25}Te_{0.25}$, and $Pb_{0.935}Na_{0.025}Cd_{0.04}Se_{0.5}S_{0.25}Te_{0.25}$ solid solutions[78]. They exhibit high ZT and low thermal conductivity.

Obviously, optimization of TE performance via the minimization in lattice thermal conductivity (κ_L) has skyrocketed. Creating a strong phonon scattering via phonon engineering is one of the best ways to minimize κ_L. This can be achieved by replacing light atoms by heaver atoms[79, 80], creating point defects[81], enhancing strong lattice anharmonicity[82], and producing dislocations[75, 83]. Thus, manipulation of the phonon dispersion is the key to reduce κ_L. The phonon dispersion in can be expressed as in Eq. (1)[84]:

$$\omega = 2\sqrt{\frac{F}{M}}\sin\left(\frac{\pi}{2}\frac{k}{k_c}\right), \tag{1}$$

where F, M, k, and k_c are the force constant, atomic mass, wave vector, and cut-off wave vector, respectively. Any manipulation of phonon dispersion can be carried out through the changes in these parameters. Low ω requires a large M but a small F (weak chemical bonds) which results in a low κ_L. Anharmonic lattice vibrations (anharmonicity) is connected to F which can be manipulated by using the elastic lattice strains, or the change to non-equilibrium atomic positions from its equilibrium position. While M can be changed through substitution, removal, or insertion of atoms. Clearly, a significant reduction in κ_L can be carried out by creating a large change in M. In the current study, we focus on the large change in M through alloying to create a significant reduction in κ_L.

There are recent studies of GeTe-based HE[66] and PbSe-based HE[77] focusing in their development and applications. Jiang et al.[66, 77] pointed out on their potential of very high ZT. In Jiang's work[66], nine GeTe-based HE solid solutions were synthesized, then TE properties such as κ_L and ZT were experimentally determined. Density

functional theory (DFT) calculations were carried out for small models with few atoms (16 atoms) by using special quasi-random structure (SQS)[85]. They calculated several mechanical parameters such as Young's modulus, shear modulus, Poisson's ratio, and Grüneisen parameter. The purpose of using SQS approach is to simulate a random solid solution using a relatively very small supercell to reduce the computational cost. However, to efficiently mimic the chemical disordering of multi-principal element in a random solid solution, using a large cell is required. Jiang et al. missed analyzing the effect of Grüneisen parameter on lattice thermal conductivity and calculating several crucial parameters such as Kleinman parameter, machinability index, Debye temperature, minimum thermal conductivity, and melting temperature.

In this study, we expand Jiang et al.'s work to fill the gap by investigating the elastic and thermal properties of pure GeTe(m0) and nine randomly disordered solid solutions of GeTe-based HE chalcogenides. They are listed in Fig. S1a, Tables S1 and S2 (shown in the supplementary information (SI)). In addition, we have investigated the pure PbSe and thirteen PbSe-based HE chalcogenide solid solutions: $Pb_{0.99-y}Sb_{0.012}Sn_ySe_{1-2x}Te_xS_x$ (x = 0.1, 0.2, 0.25, 0.3, 0.35, 0.4, 0.45, and y = 0) and $Pb_{0.99-y}Sb_{0.012}Sn_ySe_{1-2x}Te_xS_x$ (y = 0.05, 0.1, 0.15, 0.2, 0.25 and x = 0.25) as listed in Fig. S2b, Tables S3 and S4. The results are presented in "Results" section below. GeTe-based HE solid solution models each with 1080 atoms were generated from the simple rhombohedral crystal (space group $R3m$) using the supercell (SC) method[86]. Elements Ag, Sb, Pb, Bi, Cd, Cu, Sn, and Mn are distributed randomly in these nine HE models (m1 to m9). For PbSe-based HE models, thirteen solid solutions are modeled from single-phase rock-salt structure (space group fcc) with supercells each consisting of 1000 atoms. Next, the elements Sb, Sn, Te, and S are distributed randomly in these thirteen HE models. Large supercell for such HE chalcogenides are constructed for the first time in this work. Our calculations are performed using DFT-based package, *Vienna* Ab initio Simulation Package (VASP). The current methods do not consider the effect of temperature. Nevertheless, the configurational entropy is captured using randomly generated supercells. More details of the computational methods used can be found in the supplementary information (SI). The results are presented in "Results" section and discussed in "Discussion" section. Figure S1a shows Ball and stick structure of $Ge_{0.61}Ag_{0.11}Sb_{0.13}Pb_{0.12}Bi_{0.01}Te$ (m5) with their solid solution composition and model numbers in the box at right, and (b) shows Ball and stick structure of $Pb_{0.99}Sb_{0.012}Se_{0.5}Te_{0.25}S_{0.25}$ with their solid solution composition in the box on the right.

Results

Elastic constants of GeTe-based high-entropy chalcogenides

The elastic constants correlate stress to strain behavior. Elastic constants describe the response of materials under external forces. In this work, we calculated the mechanical properties of m0 and the nine GeTe-based high-entropy solid solutions models using VASP. Details of the method are described in the SI. The calculated elastic constants (C_{ij}) are listed in Table S5. They provide information about the stability, stiffness, brittleness, ductility, and anisotropy of materials. Based on the calculated C_{ij} values, m0 and nine solid solutions fulfill the mechanical stability criterial for trigonal structure[87] ($C_{11} > C_{12}$, $C_{44} > 0$, $C_{13}^2 < \frac{1}{2}C_{33}(C_{11} + C_{12})$, $C_{14}^2 < \frac{1}{2}C_{44}(C_{11} - C_{12}) \cong C_{44}C_{66}$). The elastic constants C_{11}, C_{22}, and C_{33} are strongly correlated with the unidirectional compression along the principal x, y, and z directions[88] and are very close in cubic structures. Synonymously, C_{11}, C_{22}, and C_{33} describe the resistance of a material against the deformation along [100], [010], and [001] directions, respectively, whereas the C_{44} and C_{66} measure the resistance against the shear deformation in the (100) and (001) planes, respectively. Large values of C_{11}, C_{22}, and C_{33} indicate incompressibility under uniaxial stress along x, y or z axes, respectively.

Our calculations show C_{11} and C_{22} are remarkably close in all nine solid solution models which is normal since the lattice parameters *a* and *b* are equal in the trigonal structures. The C_{11} and C_{22} for all nine solid solutions are larger than C_{33}, indicating that they are more compressible under uniaxial stress along z direction than x and y directions. It also means that the bonding strength along x and y axes are stronger than along the z axis. C_{66} is higher than C_{44} in m0, m1, m3, m5, and m8 indicating that the shear along the (100) plane is easier relative to the shear along the (001) plane. C_{44} is higher than C_{66} in m2 and m9 indicating that the shear along the (001) plane is easier relative to the shear along the (100) plane. C_{66} is higher than C_{44} in m4, m6, and m7. A low value for C_{44} indicates a high shearability. Due to the lowest C_{44} value, m5 has the highest shearability among all other solid solutions. The values of the elastic constants generally depend on the lattice parameters and the strength of the bonds between the elements. Comparing m0 (pure GeTe) with models m1 to m9, we see that introducing Ag, Sb, Pb, Bi, Cu, Mn, Cd, and Sn elements at the Ge sites led to reduction in C_{11} and C_{22}. Introducing Sb and Pb in m2; Ag, Sb, and Pb in m4; Ag, Sb, Pb, and Bi in m6; Ag, Sb, Pb, Bi, and Cu in m7; Ag, Sb, Pb, Bi, and Sn in m9 all resulted in higher value of C_{33}. Introducing Ag, Sb, Pb, and Bi in Ge sites of m5 results in much reduced elastic constants in comparison with m0, which implies that the elastic strains in m5 are much higher. Reduction of elastic strains influences their thermal conductivity.

Materials can resist the external applied stress by two ways: bond bending and bond stretching/contracting. The dimensionless Kleinman parameter (ζ)[89] can be used to determine the contribution of the bond bending or the bond stretching/contracting to resist the external stress. More information about the formula used to calculate ζ is shown in Eq. (S10). Kleinman parameter is a way to measure the stability of a material against the bending or stretching. ζ lies in the range $0 \leq \zeta \leq 1$. The lower limit of ζ indicates insignificant contribution to bond bending, whereas the upper limit of ζ means the insignificant contribution of bond stretching/contracting to resist external applied stress. The calculated ζ for m0 and the nine solid solutions models are shown in Table 1. From these values, we predict that the mechanical strength in m0 and nine solid solutions is dominated by the bond bending comparing to bond stretching/contracting.

The other mechanical parameters such as bulk modulus (K), Young's modulus (E), shear modulus (G), and Poisson's ratio (η) are obtained from the elastic coefficient C_{ij} and the compliance tensor S_{ij} ($S_{ij} = 1/C_{ij}$) using Voigt–Reuss–Hill (VRH) approximation[90, 91] for poly-crystals. They are listed in Table 1. Young's modulus

Model	E (GPa)	K (GPa)	G (GPa)	η	G/K	H_V (GPa)	H (GPa)	ζ	μ_M
m0	59.716	35.148	24.537	0.217	0.698	5.892	4.629	0.377	1.309
m1	41.484	33.447	16.038	0.293	0.480	2.849	2.214	0.539	2.217
m2	42.489	36.976	16.236	0.309	0.439	2.596	2.067	0.469	1.372
m3	47.631	32.712	18.941	0.257	0.579	3.964	3.069	0.467	1.702
m4	53.582	38.885	21.090	0.270	0.542	3.967	3.235	0.480	1.492
m5	30.362	18.626	12.359	0.228	0.664	3.425	2.242	0.433	1.741
m6	52.784	38.819	20.726	0.273	0.534	3.855	3.138	0.484	1.490
m7	52.211	38.772	20.466	0.276	0.528	3.773	3.055	0.494	1.510
m8	42.853	33.805	16.626	0.289	0.492	3.005	2.338	0.493	1.725
m9	54.603	40.317	21.425	0.274	0.531	3.922	3.229	0.478	1.400

Table 1. Young's modulus (E), bulk modulus (K), shear modulus (G), Poisson's ratio (η), Pugh's ratio (G/K), Vicker's hardness (H_V), micro-hardness (H), Kleinman parameter (ζ), and machinability index(μ_M) for ten models in Ge-Te based high-entropy chalcogenides.

measures the stiffness of the materials or change in length. Bulk modulus gives information about the resistance to compressibility or change in volume under pressure. Shear modulus represents the resistance against shear distortion. Figure S2a–d shows the distribution of K, E, G and Poisson's ration (η) of m0 and the nine HE solid solutions. m5 has the smallest K, E and G moduli. In general, introducing Ag, Sb, Pb, Bi, Cu, Mn, Cd, and Sn elements at the Ge sites results in reduced E and G. Introducing Sb and Pb in m2; Ag, Sb, and Pb in m4; Ag, Sb, Pb, and Bi in m6; Ag, Sb, Pb, Bi, and Cu in m7; Ag, Sb, Pb, Bi, and Sn in m9 resulted in higher bulk modulus comparing with m0. Eight out of the nine HE solid solutions have bulk modulus higher than 30 GPa except m5. Hence, m5 is relatively compressible in nature.

Machinability is the ease with which the materials can be machined at a low cost. The bulk modulus K together with C_{44} can control the machinability also known as machinability index (μ_M) shown in Eq. (S11). Calculating machinability index is crucial to evaluate applications in different materials. Higher μ_M indicates higher machinable characteristics. The machinability index is also a way to measure the plasticity and lubricating nature of a material[92]. It is obvious that large μ_M requires a small C_{44} which can give a better dry lubricity. Large value of μ_M leads to lower friction and higher plastic strain. Solid solutions models m1, m5, and m8 have the largest values of μ_M among others as shown in Table 1. The ratio of shear modulus to bulk modulus (G/K), or Pugh's modulus ratio[91, 93] is an useful parameter that determines the brittle and ductile behaviors of materials. G/K for m0 and other nine HE solid solution models are listed in Table 1 and shown in Fig. S3a. According to Pugh's criterion, materials with G/K larger than 0.571 tend to be brittle and those less than 0.571 tend to be ductile[93, 94]. Similarly, m0, m3, and m5 are brittle while the remaining models are more ductile. Another rule to characterize material's brittleness or ductility is the Frantsevich's rule of Poisson's ratio[95]. It assumes that if Poisson's ratio (η) is less than 0.26, the material tends to be brittle otherwise, it is ductile. Hence, Frantsevich's rule and Pugh's criterion are equivalent.

We also used Vicker's hardness or macro hardness (H_V) formula to calculate the hardness (H_V) of m0 and other nine solid solutions models. Vicker's hardness formula was formulated by Chen et al.[96] and Tian et al.[97]. Vicker's hardness formula was derived from the elastic constants[98–100] using Eq. (S12). The calculated values of H_V for m0 and all nine solid solution models are listed in Table 1. Figure S3b shows the distribution of the Vicker's hardness of m0 and the nine HE solid solutions. Materials with Hv larger than 40 GPa are presumed to be super hard materials[101]. H_V of the 10 models listed in Table 1 have values less than 10 GPa and cannot be considered as hard materials. Historically, Macro Vickers loads vary from 2 to 120 kg. However, when the applied loads range from a few grams to several kilograms, micro-hardness (H) measurements are more suitable[102, 103]. A semi-empirical formula that can estimate the micro-hardness (H) is listed in Eq. (S13). The values of H are listed in Table 1. Both macro hardness (H_V) and micro hardness (H) have the same trend and both of them are crucial parameters to be calculated for the chalcogenide models. From the above results, introducing Ag, Sb, Pb, Bi, Cu, Mn, Cd, and Sn elements at the Ge sites results in reduced brittleness and hardness of the nine solid solution models.

Another popular parameter used to classify the chemical bonding of a material is the Cauchy pressure (CP)[104, 105]. CP for trigonal structures can be calculated using following formula: $CP_x = C_{13} - C_{44}$ and $CP_y = C_{12} - C_{66}$[104]. A negative CP indicates dominance of covalent bonding and a positive CP indicates dominance of ionic bonding[106]. As shown in Table S6, the covalent bonding is dominant in m0 and m5 and the ionic bonding is dominant in m1, m7, and m8. The remaining models (m2, m3, m4, m6, and m9) have mixed nature of both ionic and covalent bonding due to the opposite signs of CP_x and CP_y. Cauchy pressure can also be used to predict the brittle/ductile behavior of materials. Negative CP implies that the material is brittle. m0, m3, and m5 have negative CP so they are brittle. This result is in agreement with Pugh's criterion. The elasticity's response was also investigated by us through the Lame's constants (λ, μ). Lame's constants can be used to measure the compressibility and the shear stiffness of a material, respectively. In most cases, and in the context of elasticity, μ carries the same information as shear modulus. The formula used to calculate λ and μ can be found in Eqs. (S14) and (S15). λ can be negative, while μ is always positive. The values of λ and μ at zero temperature and zero pressure are listed in Table S6. As can be seen, m0 and m5 exhibit shear stiffness than compressibility, while the other solid solutions models exhibit opposite trends.

The elastic anisotropy parameter is characterized by the universal anisotropic index (A^U) calculated using formula (S16), listed in Table S7, and shown in Fig. S3c. If A^U has a value of unity, the material is isotropic, while values other than unity give varying degrees of anisotropy[107]. The A^U for m0 and all nine models vary from unity in different degrees, showing their anisotropic nature. Comparatively, m3 has A^U close to 1 showing isotropic nature. Another way of measuring the elastic anisotropy is the percentage of anisotropy in compression (A_{comp}) and shear (A_{shear}) listed in Table S7. If A_{comp} and A_{shear} have a value of zero, it indicates isotropic elastic behavior whereas their value of 1 indicates largest possible anisotropy. The shear anisotropic factor for {100} shear planes between the [011] and [010] directions (A_1), the shear anisotropic factor for {010} shear planes between the [101] and [001] directions (A_2), and the shear anisotropic factor for {001} shear planes between the [110] and [010] directions (A_3) are calculated by the formulae (S19), (S20) and (S21). The values of A_1, A_2, and A_3 for m0 and nine solid solution models are presented in Table S7. If $A_1 = A_2 = A_3 = 1$, the material is isotropic and bonds existing between the planes, otherwise, the opposite is true, or anisotropic nature for all models.

The directional dependent mechanical properties, E, K in terms of compressibility (1/K), G, and η, are presented in three-dimensional (3D) surface plots via ELATE program[108] in Figs. S4–S7 respectively. The isotropic compounds exhibit a perfect spherical in 3D plot. The 3D surface plot of E (Fig. S4) and G (Fig. S6) shows m0 and all nine solid solution models are anisotropic nature. m1 and m5 have less deviation while m2 has the largest deviation from the spherical shape for both E and G, indicating that m2 has the highest Young and shear anisotropy while m1 and m5 have the least. An extreme anisotropy in the compressibility (inversely proportional to the bulk modulus) is notable in all nine solid solution models. The circular graphic in 2D for elastic moduli gives the same information about the isotropic nature of solids. The amount of deviation from the circular shape determines the degree of anisotropy. Figures S8–S17 show the two-dimensional (2D) plots of E, 1/K, G, and η for m0 and other nine solid solutions. Figures S8–S17 show that E and 1/K are found to be isotropic in the xy plane while they are anisotropic in xz and yz planes for all models. The minimum and maximum values of each mechanical modulus derived by using ELATE program are listed in Table S8.
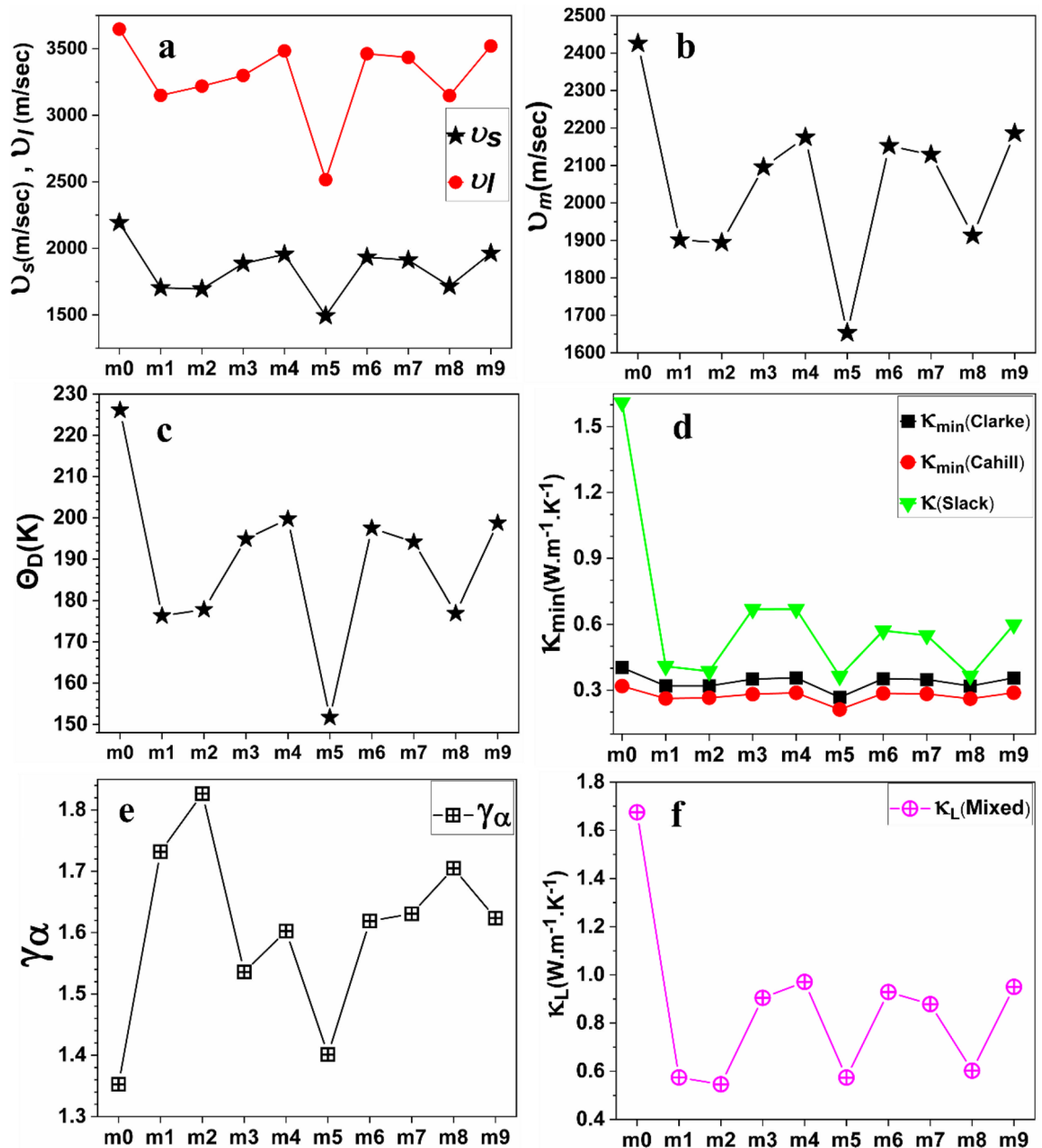
Debye temperature and thermal conductivity of GeTe-based high-entropy chalcogenides

Debye temperature (Θ_D) originates from the theory of thermal vibration of atoms. Θ_D in condensed materials can reflect the strength of covalent bonding and other thermal characteristics such as specific heat, melting temperature, and thermal expansion. Θ_D is positively correlated with thermal conductivity (κ) and is an important parameter in high temperature applications. Anderson's method is one of the straightforward and accurate methods to calculate Θ_D. The formula used to calculate Θ_D is shown in Eq. (S22). Other parameters used to calculate Θ_D, such as the average sound velocity (v_m), the transverse (shear) velocity (v_s), and the longitudinal sound velocity (v_l) are shown in Eqs. (S23), (S24) and (S25) respectively. The calculated v_s, v_l, v_m, and Θ_D for m0 and the nine solid solution models are listed in Table 2 and plotted in Fig. 1a–c. We notice that m0 has the highest Θ_D and v_m, while m5 has the smallest v_m and Θ_D. This indicates that m5 has the weakest bond strength and lowest thermal conductivity. m1, m2, and m8 have close values of v_m and Θ_D. Materials with low Θ_D tend to be soft materials with low melting temperature. While materials with higher Θ_D tend to be harder, with stronger interatomic bonding and higher melting temperature[109, 110]. From Table 2, we notice that the transverse sound velocity v_s is depressed in all nine solid solution models (form m1 to m9) in comparison to pure GeTe (m0). m2 and m5 have the smallest values of v_s. This significantly dampened transverse phonon modes (v_s) would strengthen the scattering of phonons[111] which in return results in a reduced lattice thermal conductivity (κ_L). Impedance parameter (Z) is used in acoustic applications such as noise reduction and transducer design. In this work, Z is calculated using Eq. (S26) and listed in Table 2. When sound waves are transmitted, the difference in Z between two materials determines the amount of acoustic energy transmitted at their interface.

Thermal conductivity (κ) measures the performance of heat transfer at high temperatures[112]. It is crucial to calculate the minimum thermal conductivity (κ_{min}) and lattice thermal conductivity (κ_L) since they determine the TE performance. Clarke's model[113], Cahill's model[114], and Slack's model[115] were used to estimate κ_{min} and κ of m0 and other nine HE chalcogenide solid solutions at 300 K. The formulae (S27), (S28), (S29) and (S31) were

Model	ρ (Kg/m³)	v_s (m/sec)	v_l (m/sec)	v_m (m/sec)	Θ_D (K)	Z (× 10⁶)
m0	5100.85	2193.257	3647.526	2425.743	226.102	11.187
m1	5526.86	1703.475	3149.734	1901.120	176.298	9.415
m2	5658.40	1693.919	3218.777	1894.103	177.805	9.585
m3	5326.40	1885.752	3298.924	2095.333	194.876	10.044
m4	5521.33	1954.413	3483.628	2175.012	199.725	10.791
m5	5546.19	1492.775	2515.852	1653.128	151.689	8.279
m6	5545.39	1933.267	3461.732	2152.272	197.491	10.721
m7	5600.65	1911.601	3434.394	2128.719	194.132	10.706
m8	5651.86	1715.135	3146.978	1913.041	176.884	9.694
m9	5558.50	1963.277	3520.297	2185.922	198.754	10.913

Table 2. The theoretical density (ρ), the calculated sound velocity (longitudinal v_l, transverse v_s, and average v_m), Debye temperature Θ_D, and the acoustic impedance (Z) in Kg m⁻² s⁻¹ unit for ten models in Ge-Te based high-entropy chalcogenides.

Figure 1. (**a**) Longitudinal v_l and transverse v_s velocities, (**b**) Average sound velocity, (**c**) Debye temperature, (**d**) thermal conductivities at 300 K, (**e**) Acoustic Grüneisen constant, and (**f**) Lattice thermal conductivities calculated according to mixed model at 300 K for the ten models in Ge-Te based high-entropy chalcogenides.

used to calculated κ_{min}, κ, and Grüneisen constant (γ_α) respectively. They are listed in Table 3. Figure 1d shows that m5 has the lowest κ_{min} according to Clarke's model and Cahill's model, while m2, m5, and m8 have the lowest and comparable values of κ according to Slack's model. The Grüneisen constant γ_α provides information about the nature of materials by measuring the bond anharmonicity, which is related to the interatomic interaction[116]. If γ_α is large, the anharmonic vibrations are strong, indicating a small influence of temperature increase on the lattice dynamics and thermal properties. The calculated γ_α for m0 and other nine HE chalcogenide solid solutions are summarized in Table 3 and Fig. 1e. With the lowest γ_α, m0 and m5 are the highest influenced under high temperature (higher and temperature-dependent lattice thermal conductivity) whereas m2 with highest γ_α is less influenced under high temperature (depressed and temperature-independent lattice thermal conductivity). However, strong anharmonic vibrations (higher γ_α) also indicate higher phonon scattering and thus low κ. Hence, according to this criterion, m5 should have the highest value of γ_α among other models. Another formula that estimates Grüneisen parameter using the Poisson's ratio is shown in Eq. (S32). Poisson's ratio can be calculated using the transverse (v_s) and the longitudinal (v_l) sound velocities as shown in Eq. (S33). v_s and v_l can also be estimated using the elastic constants as shown in Eqs. (2) and (3) below[117]:

Model	Clarke model κ_{min} (W.m^{-1}.K^{-1})	Cahill model κ_{min} (W.m^{-1}.K^{-1})	Slack model κ (W.m^{-1}.K^{-1})	A ($\times 10^{-6}$)	Slack model κ_A (W.m^{-1}.K^{-1})	γ_α Eq. (S31)	γ_α Eq. (S32)
m0	0.4028	0.3185	1.610	3.2632	1.695	1.3526	1.6424
m1	0.3193	0.2620	0.409	3.1190	0.411	1.7319	2.1978
m2	0.3193	0.2652	0.386	3.0869	0.384	1.8266	1.3132
m3	0.3505	0.2815	0.669	3.1897	0.688	1.5358	1.8898
m4	0.3560	0.2878	0.670	3.1645	0.683	1.6026	1.4747
m5	0.2670	0.2119	0.364	3.2437	0.381	1.4011	2.2736
m6	0.3520	0.2851	0.571	3.1586	0.582	1.6189	1.4439
m7	0.3486	0.2828	0.550	3.1528	0.559	1.6307	1.4561
m8	0.3190	0.2609	0.366	3.1271	0.369	1.7049	1.6818
m9	0.3558	0.2883	0.599	3.1567	0.609	1.6237	1.3085

Table 3. The calculated minimum thermal (κ_{min}) and thermal (κ) conductivities (W·m^{-1}. K^{-1}) at 300 K, the constant A (A here is calculated by using the Julian's formula (S34)), Slack's thermal conductivity (κ_A) calculated by using the constant A in the fifth column, Grüneisen parameter (γ_a) calculated by using the formula (S31), and Grüneisen parameter calculated by using the formula (S32) for ten models in Ge-Te based high-entropy chalcogenides.

$$v_l = \sqrt{\frac{C_{11}}{\rho}}, \tag{2}$$

$$v_s = \sqrt{\frac{C_{44}}{\rho}}, \tag{3}$$

The calculated v_l and v_s (using Eqs. (2) and (3) respectively), and η (using Eq. (S33)) are listed in Table S9. The calculated γ_α (using Eq. (S32)) are listed in Table 3. m5 has the highest γ_α which agrees well with its lowest value of κ.

In Fig. S18, we plotted the v_l/v_s versus Grüneisen parameter, showing that Gruneisen parameter is linearly proportional to v_l/v_s. The increasing v_l/v_s on x-axis implies a decrease in v_s. The decrease in v_s from the softened transverse phonons is the reason for the increase of γ_α (Eq. S31). Thus, the anharmonicity (γ_α), which describes the interactions among the different branches of phonons, is largely strengthened, resulting in a temperature-independent and significantly reduced κ_L. Thermal conductivity (κ) calculated by Slack's formula (Eq. S29) consists of a constant A. A well-known value of A is 3.1e–6. However, for better accuracy, Julian derived a formula for the constant A (shown in Eq. (S34)). The A values listed in the fifth column of Table 3 result in slightly different values of Slack's thermal conductivity (κ_A) shown in the sixth column of Table 3 for all solid solutions models.

At low temperatures, the electron–phonon scattering is small. Thus, thermal conductivity κ is mainly contributed by lattice thermal conductivity κ_L. κ_L has a relatively small values at low temperatures. κ_L has contributions from acoustic phonons (κ_a) and optical phonons (κ_o). It is crucial to calculate κ_L to ascertain whether the HE chalcogenides considered are good TE materials or not. We have calculated κ_L, κ_a, and κ_o using the Eqs. (S35), (S36) and (S37) respectively. Table 4 lists their values at 300 K. Figure 1f shows that m2, m5, and m8 have the lower κ_L among all other HE solid solutions. The Callaway-Debye theoretical model[118] states that a higher Θ_D indicates a higher thermal conductivity and vice versa. We plotted Θ_D versus κ in Fig. S19a–d in SI to reveal the correlation between Θ_D and κ. Figure S19 shows that Θ_D is positively correlated with κ in agreement with Callaway-Debye model. The comparison between our calculated κ and κ_L with the experimental lattice thermal conductivity (κ_L)$_{exp}$

Model	Mixed model κ_L (W.m^{-1}.K^{-1})	Mixed model κ_a (W.m^{-1}.K^{-1})	Mixed model κ_o (W.m^{-1}.K^{-1})
m0	1.6750	1.5899	0.0851
m1	0.5743	0.5083	0.0660
m2	0.5457	0.4800	0.0658
m3	0.9048	0.8316	0.0732
m4	0.9708	0.8967	0.0741
m5	0.5740	0.5178	0.0562
m6	0.9290	0.8558	0.0732
m7	0.8963	0.8239	0.0725
m8	0.6142	0.5482	0.0661
m9	0.9696	0.8956	0.0740

Table 4. Lattice thermal conductivities κ_L (W·m^{-1}. K^{-1}) at 300 K calculated by using mixed model, κ_L contributed by acoustic phonons (κ_a), and κ_L contributed by optical phonons (κ_o) for ten models in Ge-Te based high-entropy chalcogenides.

from Jiang's work[66] is listed in Table S10 showing similar trends. Melting temperature (T_{melt}) is correlated to Θ_D, κ_L, and thermal expansion. Materials with low T_{melt} tend to have lower Θ_D and higher thermal expansion. For high temperature applications such as thermoelectric applications, it is crucial to identify the thermal limits or melting temperature (T_{melt}) of a material. More information about the formula used to calculate T_{melt} can be found in (S38). The calculated T_{melt} for m0 and nine solid solutions are presented in Table S10. m1, m5, and m8 have the lowest T_{melt}. Thermal expansion is the tendency of material to change the shape, volume, and density in response to a change in temperature. Thermal expansion is designated by thermal expansion coefficient (α). α for m0 and nine solid solutions can be estimated from the formula (S39). Table S10 shows that m1 and m5 have the largest α. The lattice vibrations in materials have a huge contribution to several physical properties, such as electrical conductivity, thermo-power, and thermal conductivity. The wavelength at which the heat phonon spectra or the phonon energy distribution curve strikes its maximum value is called the dominant phonon wavelength (λ_{dom}).

Dominant phonon wavelength carries the majority of heat in most materials. It is important to calculate λ_{dom} to identify the total energy of phonons or the maximum energy of phonons at a certain temperature. λ_{dom} and the mean free path (MFP) (the average distance that a phonon travels between two successive inelastic collisions) are positively correlated. These two parameters play a significant role in controlling κ_L. Shifting the heat phonon spectra towards shorter wavelengths (smaller λ_{dom}) and shorter mean free paths may increase the scattering of phonons and reduce κ_L[119]. λ_{dom} can be roughly estimated at 300 K by using the formula (S40). The calculated λ_{dom} for m0 and nine solid solutions are represented in Table S10. λ_{dom} has been shortened from 1.02 Å for m0 to 0.692 Å for m5 which indicates that the phonon heat spectra are strongly modified by HE alloying.

PbSe-based high-entropy chalcogenides

$Pb_{0.99-y}Sb_{0.012}Sn_ySe_{1-2x}Te_xS_x$ (x = 0.1, 0.2, 0.25, 0.3, 0.35, 0.4, 0.45, with y = 0) solid solutions
In this section, we focus on results of solid solutions $Pb_{0.99-y}Sb_{0.012}Sn_ySe_{1-2x}Te_xS_x$ (x = 0.1, 0.2, 0.25, 0.3, 0.35, 0.4, 0.45, and y = 0). The calculated elastic constants of pure PbSe and eight solid solutions are listed in Table S11. Some of these results are also shown in Fig. 2a and b. Figure 2a shows a sharp reduction of C_{11}, C_{22}, and C_{33} of $Pb_{0.99-y}Sb_{0.012}Sn_ySe_{1-2x}Te_xS_x$ (with y = 0 and x = 0.25) or $Pb_{0.99}Sb_{0.012}Se_{0.5}Te_{0.25}S_{0.25}$. With increase of x content, a gradual reduction of C_{44}, C_{55}, and C_{66} is observed in Fig. 2b. The reduction of elastic constants with increase of x content implies an increase of the elastic strains. PbSe-based HE solid solution models have a cubic structure. Thus, a different empirical formula shown in Eq. (S41) was used to estimate the melting temperature (T_{melt}) of both $Pb_{0.99-y}Sb_{0.012}Sn_ySe_{1-2x}Te_xS_x$(x = 0.1, 0.2, 0.25, 0.3, 0.35, 0.4, 0.45, and y = 0) and $Pb_{0.99-y}Sb_{0.012}Sn_ySe_{1-2x}Te_xS_x$(y = 0.00, 0.05, 0.10, 0.15, 0.20, 0.25, and x = 0.25). The theoretical density (ρ), the calculated sound velocity (longitudinal v_l, transverse v_s, and average v_m), Θ_D, T_{melt}, α, and λ_{dom} for $Pb_{0.99-y}Sb_{0.012}Sn_ySe_{1-2x}Te_xS_x$ ((x = 0.1, 0.2, 0.25, 0.3, 0.35, 0.4, 0.45) and y = 0) solid solutions are listed in Table S12. In general, λ_{dom} has been shortened for all models. λ_{dom} has been shortened from its highest value(0.890 Å) in pure PbSe to its lowest value(0.718 Å) for $Pb_{0.99}Sb_{0.012}Se_{0.5}Te_{0.25}S_{0.25}$ model. Shortening λ_{dom} reduces the mean free path of phonons which increases scattering of phonons resulting in a reduced κ_L.

Figure 2c–f depict the calculated v_m, Θ_D. T_{melt}, and α versus x content of $Pb_{0.99-y}Sb_{0.012}Sn_ySe_{1-2x}Te_xS_x$. v_m, Θ_D, and T_{melt} decreases with increase of x content. The same trend is noticed for elastic constants. While thermal expansion increases with increase of x content, a sharp reduction in v_m, Θ_D, and T_{melt} is notable for $Pb_{0.99-y}Sb_{0.012}Sn_ySe_{1-2x}Te_xS_x$ (with y = 0 and x = 0.25) or $Pb_{0.99}Sb_{0.012}Se_{0.5}Te_{0.25}S_{0.25}$ (the same trend is common with elastic constants C_{11}, C_{22}, and C_{33}). A sharp increase of α is noted for $Pb_{0.99}Sb_{0.012}Se_{0.5}Te_{0.25}S_{0.25}$. Lower v_m and Θ_D indicates weaker chemical bonds and a lower κ_L. The reduction in v_m with increase of x content is large in the current study (see Fig. 2c). A small decrease in v_m corresponds to large decrease in κ_L. The large reduction in Θ_D with increase of x content (see Fig. 2d) indicates weaker chemical bonds which results in higher anharmonicity or higher Grüneisen parameter, thus higher phonon scattering and lower κ_L. Clearly, increasing x content results in higher strains or lower elastic constants. Thus, the sound velocities or phonon velocities (longitudinal (v_l) and transverse (v_s)) decrease.

This can be understood via the correlation between the phonon velocity and the elastic constants shown in Eqs. (2) and (3). Reducing the sound or phonon velocity via increasing the strains is one of the engineering methods for reducing κ_L and consequently enhancing the TE performance. Phonon velocities and κ_L are correlated by the Eq. (4)[120]:

$$\kappa_{ij} = \sum_{\alpha} C_{\alpha} \tau_{\alpha} v_i v_j, \tag{4}$$

where C_{α}, τ_{α}, and v are the heat capacity, phonon scattering time or relaxation time, and phonon velocity, respectively. *i*, *j* refers to the three principal axes of the chosen coordinate system. The element substitution creates a disorder by modify the atomic positions. Thus, weak displacements of the atoms and bonds were produced, resulting in enhancement of bond anharmonicity which results in higher γ_{α}. Figure 3a shows the Grüneisen parameter increases with increase of x content of $Pb_{0.99-y}Sb_{0.012}Sn_ySe_{1-2x}Te_xS_x$, which results in a reduced κ_L (see Fig. 3c). Figure 3b and c show κ_{min} and κ_L are reduced with increase of x content. This is an evidence of elastic strain's effect on thermal conductivity. The calculated thermal conductivities and Grüneisen parameter of $Pb_{0.99-y}Sb_{0.012}Sn_ySe_{1-2x}Te_xS_x$ models are listed in Table 5.

The calculated Young's modulus (E), bulk modulus (K), shear modulus (G), Poisson's ratio (η), Pugh's ratio (G/K), Vicker's hardness (H_V), Kleinman parameter(ζ), machinability index(μ_M), Cauchy pressures (CP), and Lame's constants (λ, μ) for $Pb_{0.99-y}Sb_{0.012}Sn_ySe_{1-2x}Te_xS_x$ solid solutions (x = 0.1, 0.2, 0.25, 0.3, 0.35, 0.4, 0.45) and y = 0 are listed in Table S13. Grüneisen parameter versus v_l/v_s plot is shown in Fig. S20 which has a positive correlation similar to GeTe and its solid solutions. Figure S21a–d shows the distribution of the E, K, G, and η of $Pb_{0.99-y}Sb_{0.012}Sn_ySe_{1-2x}Te_xS_x$ versus x content. As can be seen, there is a gradual reduction of E, K, and G for all solid solution models with increase of x content with a notable sharp reduction with y = 0 and x = 0.25. On the other hand, Poisson's ration increases with increase of x content. A gradual increase of the machinability
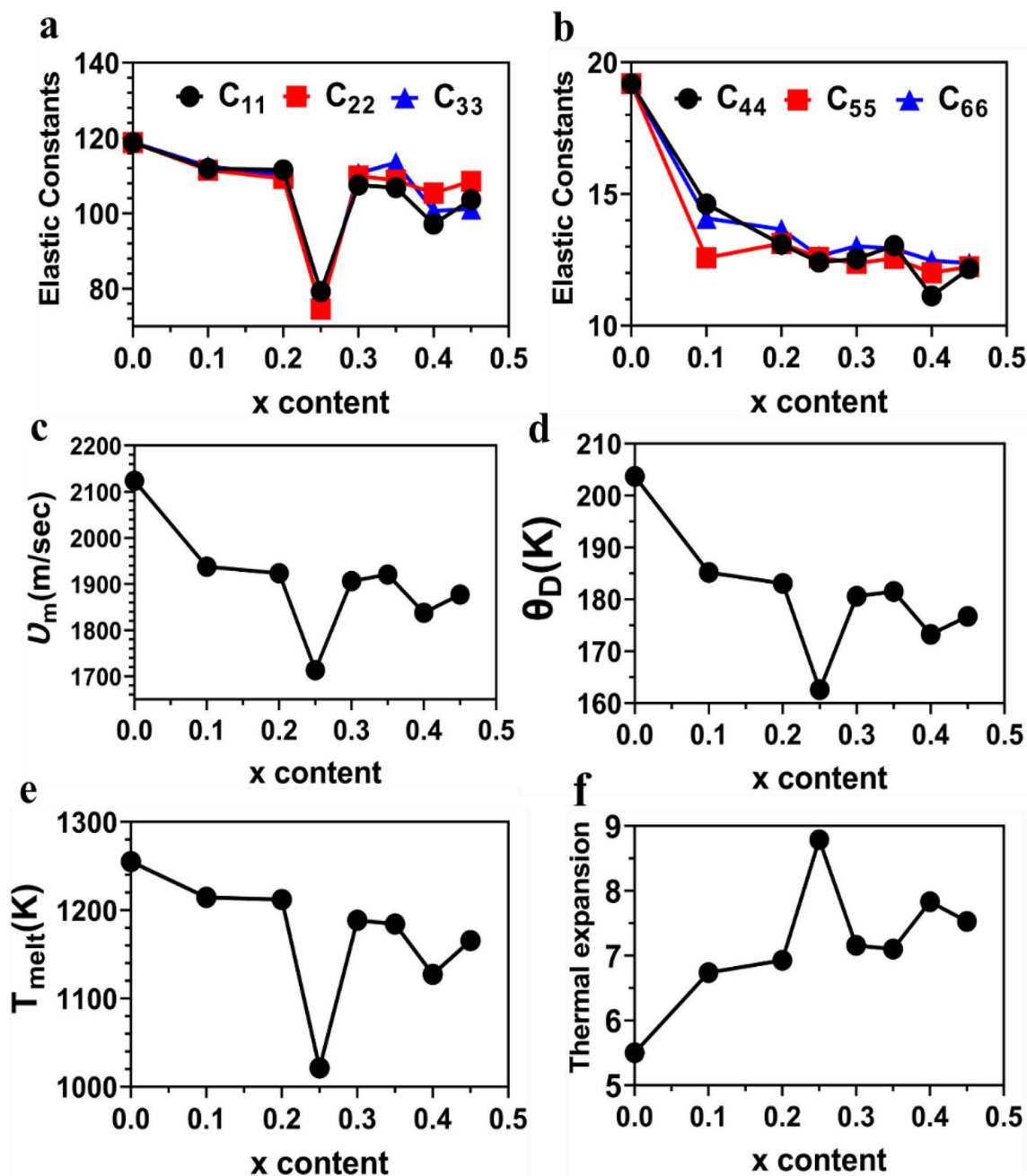
Figure 2. (**a**)The distribution of the elastic constants C_{11}, C_{22}, C_{33}, (**b**) C_{44}, C_{55}, C_{66}, (**c**) Average sound velocity, (**d**) Debye temperature, (**e**) melting temperature, and (**f**) thermal expansion of $Pb_{0.99-y}Sb_{0.012}Sn_ySe_{1-2x}Te_xS_x$ solid solution models with respect of x content (x = 0.1, 0.2, 0.25, 0.3, 0.35, 0.4, 0.45) and y = 0.

index for all solid solution models with increase of x content, with a notable dip at 0.25 × content in Fig. S22a. In Fig. S22b, the first Lame's constant (λ) is larger than the second Lame's constant (μ) for all solid solutions models indicating a higher compressibility than shear.

Pugh's ratio (G/K) is also listed in Table S13. All solid solution models tend to be ductile, except pure PbSe which tends to be brittle. Cauchy pressure (CP) is calculated by using the formula: $(C_{12}-C_{44})$[121]. The calculated CP of $Pb_{0.99-y}Sb_{0.012}Sn_ySe_{1-2x}Te_xS_x$ versus x (x = 0.1, 0.2, 0.25, 0.3, 0.35, 0.4, 0.45) and y = 0 are listed in Table S13. Large positive CP value is noted for $Pb_{0.99-y}Sb_{0.012}Sn_ySe_{1-2x}Te_xS_x$ (x = 0.25, y = 0) or $Pb_{0.99}Sb_{0.012}Se_{0.5}Te_{0.25}S_{0.25}$ which indicates dominant ionic bonds. The calculated A^U, G_V, G_R, K_V, and V_R are given in Table S14. A^U of $Pb_{0.99-y}Sb_{0.012}Sn_ySe_{1-2x}Te_xS_x$ varies from unity in different degrees. However, $Pb_{0.99-y}Sb_{0.012}Sn_ySe_{1-2x}Te_xS_x$ (x = 0.25, y = 0) or $Pb_{0.99}Sb_{0.012}Se_{0.5}Te_{0.25}S_{0.25}$ shows isotropic nature compared to other solid solutions.
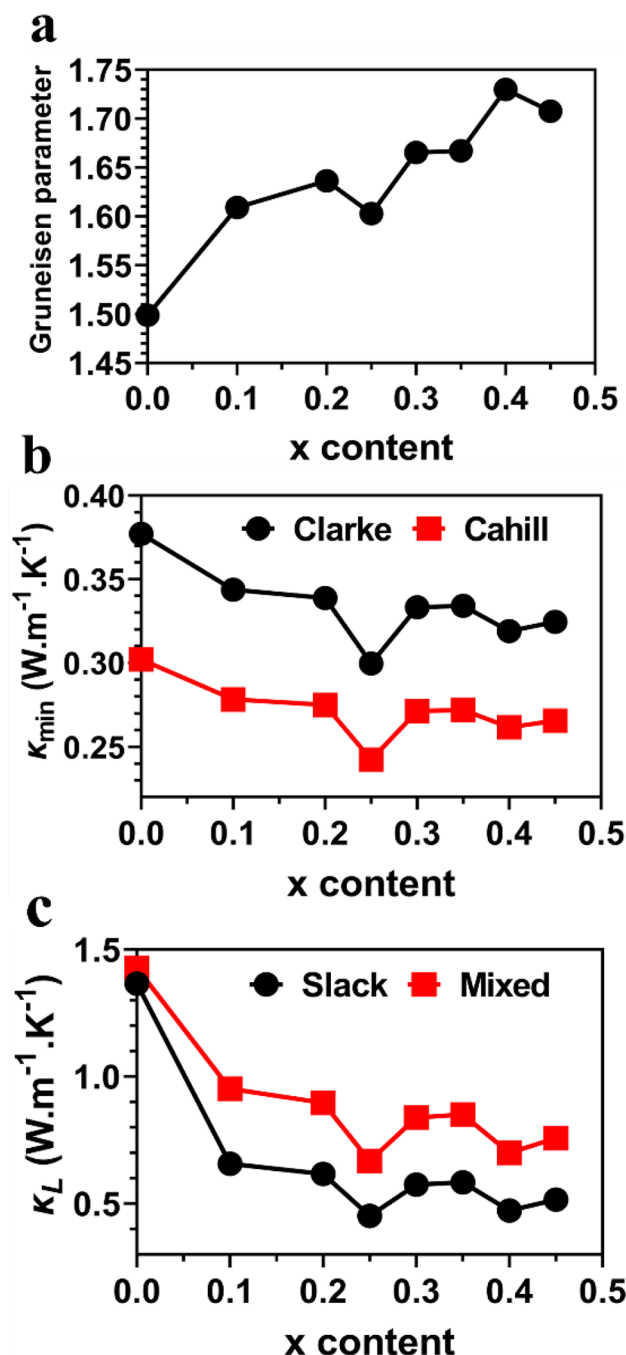
Figure 3. (**a**) Acoustic Grüneisen constant, (**b**) Minimum thermal conductivities, and (**c**) Lattice thermal conductivities at 300 K for $Pb_{0.99-y}Sb_{0.012}Sn_ySe_{1-2x}Te_xS_x$ solid solution models with respect to x content with y = 0.

$Pb_{0.99-y}Sb_{0.012}Sn_ySe_{1-2x}Te_xS_x$ (y = 0.0, 0.05, 0.1, 0.15, 0.2, 0.25, and x = 0.25) solid solutions

In this section, we focus on results of solid solutions $Pb_{0.99-y}Sb_{0.012}Sn_ySe_{1-2x}Te_xS_x$ (y = 0.0, 0.05, 0.1, 0.15, 0.2, 0.25, and x = 0.25). The calculated elastic constants, Young's modulus, bulk and shear moduli, Poisson's ration, Vicker's hardness, Kleinman parameter, machinability index, Cauchy pressure, Lame's constants, and the universal anisotropic index of $Pb_{0.99-y}Sb_{0.012}Sn_ySe_{1-2x}Te_xS_x$ (y = 0.0, 0.05, 0.1, 0.15, 0.2, 0.25, and x = 0.25) solid solutions are listed in Tables S16, S17, S18 and S19. Figure S23a to d show the calculated v_m, Θ_D, T_{melt}, and α versus y content of $Pb_{0.99-y}Sb_{0.012}Sn_ySe_{1-2x}Te_xS_x$(y = 0.0, 0.05, 0.1, 0.15, 0.2, 0.25) and x = 0.25. The first model: $Pb_{0.99-y}Sb_{0.012}Sn_ySe_{1-2x}Te_xS_x$ (y = 0.0, x = 0.25) is discussed in the previous section. It is noticed that v_m and Θ_D have a sharp peak at y = 0.05 and then a gradual decrease with the increase in y content. A sharp reduction in T_{melt} is notable for $Pb_{0.99-y}Sb_{0.012}Sn_ySe_{1-2x}Te_xS_x$ (with y = 0.1 and x = 0.25). Thermal expansion coefficient has a sharp decrease at y = 0.05 and y = 0.1 and then gradually increases. Clearly, increasing y content while keeping x = 0.25 results in lower v_m, Θ_D, and T_{melt}. The calculated thermal conductivities and Grüneisen parameter of

x	Clarke model κ_{min} (W.m⁻¹.K⁻¹)	Cahill model κ_{min} (W.m⁻¹.K⁻¹)	Slack model κ (W.m⁻¹.K⁻¹)	Mixed model κ_L (W.m⁻¹.K⁻¹)	κ_a (W.m⁻¹.K⁻¹)	κ_o (W.m⁻¹.K⁻¹)	γ_a
–	0.3772	0.3019	1.3656	1.4273	1.3484	0.0789	1.499
0.10	0.3437	0.2781	0.6566	0.9510	0.8795	0.0715	1.609
0.20	0.3388	0.2749	0.6164	0.8961	0.8258	0.0703	1.636
0.25	0.2996	0.2423	0.4517	0.6675	0.6051	0.0623	1.603
0.30	0.3331	0.2712	0.5744	0.8385	0.7694	0.0691	1.665
0.35	0.3340	0.2720	0.5835	0.8509	0.7816	0.0693	1.667
0.40	0.3189	0.2617	0.4726	0.6991	0.6331	0.0659	1.730
0.45	0.3245	0.2655	0.5156	0.7578	0.6907	0.0672	1.708

Table 5. Calculated thermal (κ) and minimum thermal (κ_{min}) conductivities (W·m⁻¹. K⁻¹) at 300 K, lattice thermal conductivities κ_L (W·m⁻¹. K⁻¹) at 300 K, κ_L contributed by acoustic phonons (κ_a), and κ_L contributed by optical phonons (κ_o), and Grüneisen parameter (γ_a) for pure PbSe and $Pb_{0.99-y}Sb_{0.012}Sn_ySe_{1-2x}Te_xS_x$ solid solutions.

$Pb_{0.99-y}Sb_{0.012}Sn_ySe_{1-2x}Te_xS_x$ (($y = 0.0, 0.05, 0.1, 0.15, 0.2, 0.25$) with $x = 0.25$) are listed in Table S20. The calculated density (ρ), v_l, v_s, v_m, Θ_D, T_{melt}, α, and λ_{dom}(Å) for $Pb_{0.99-y}Sb_{0.012}Sn_ySe_{1-2x}Te_xS_x$ (($y = 0.0, 0.05, 0.1, 0.15, 0.2, 0.25$) and $x = 0.25$) are listed in Table S21. In Fig. S24a, we notice the Grüneisen parameter of $Pb_{0.99-y}Sb_{0.012}Sn_ySe_{1-2x}Te_xS_x$ has a notable dip at 0.1 y-content and then increasing rapidly with increase of y content. In Fig. S24b, κ_{min} starts to increase till 0.05 of y-content and then gradually decreases thereafter. In Fig. S25, κ_L starts to increase till 0.1 y-content and then decreases thereafter. y-content above 0.1 in $Pb_{0.99-y}Sb_{0.012}Sn_ySe_{1-2x}Te_xS_x$ ($x = 0.25$) models results in much higher Grüneisen parameter and consequently, a reduced κ_L.

Discussion

In GeTe-based HE models, Alloying by Pb and Bi atoms at the Ge atom sites produced higher mass and strain field fluctuations to scatter phonons due to the larger atomic size and heavier mass of Bi and Pb than Ge. This may be the main reason for the lower κ_L in most nine HE models under study. Furthermore, the alloy defects may have strengthened the phonon scattering, resulting in much depressed κ_L. Our results for κ_L show the same trend as the experimental data of Jiang et al.[66]. Materials with low Θ_D and low thermal conductivity have remarkable applications as TE and thermal barrier coatings (TBC) materials. We revealed that there is a positive correlation between Debye temperature and thermal conductivity for the investigated nine HE models. A strong anharmonicity (high Grüneisen parameter) indicates weak atomic bonds, and thus low κ_L[122, 123]. There is a positive correlation between sound velocity and the strength of interatomic interactions. Lower sound velocity indicates weaker interatomic interactions between atoms as indicated by large Grüneisen parameter[124]. We know from Eq. (4) that κ_L can be reduced by minimizing three parameters: heat capacity (C_a), phonon relaxation time (τ_a), and phonon velocity (υ). If the speed of sound (i.e. lattice stiffness) can be manipulated via some methods, κ_L can be reduced significantly. One of the techniques for reducing speed of sound is inducing internal-strain fields, which are induced by lattice defects such as dislocations, alloying, and doping[125]. Internal- strains change the speed of sound which results in higher phonon scattering and lower κ_L. At small strains, the phonon frequency (ω) and the speed of sound, the Grüneisen tensor (γ_{ij}), and the strain tensor (ε_{ij}) are correlated by the following formula[126]:

$$\omega = \omega_0 (1 - \gamma_{ij}\varepsilon_{ij}), \tag{5}$$

where ω_0 is the phonon frequency at zero strain. Clearly, increasing γ and ε will reduce the phonon frequency and thus reduce κ_L. Compared to m0 (pure GeTe), the lattice parameters have been increased in m5 ($Ge_{0.61}Ag_{0.11}Sb_{0.13}Pb_{0.12}Bi_{0.01}Te$) due to the alloying (see Table S2), which indicates an increase in atomic separation distances. This increase in atomic separation distances weakens the chemical bond strength between atoms, thereby elastic constants significantly decreased in m5 (see Table S5). m5 has been softened (much lower Young's modulus, bulk and shear moduli) due to the weak bond strength (see Table 1). Softening the chemical bonds also decreases phonon group velocity (see Table 2 for m5 model). The dramatic change of the values of elastic properties in m5 indicates that the deformation resistance of this model has a significant change. The current DFT calculations cannot fully explain the reason behind the increase of elastic properties when alloying with a small fraction of element Cu in m6 ($Ge_{0.61}Ag_{0.11}Sb_{0.13}Pb_{0.12}Bi_{0.01}Cu_{0.003}Te$), subsequent to their suppression in m5. Multiple elements alloying introduces atomic disorder (either substitutionally or interstitially) in the HE model lattice, which in general is considered as point defects. Alloying also causes severe lattice distortion which together with the point defects are favorable for dislocation formation[127]. This results in a strong strain field to reduce lattice thermal conductivity. Dislocations can significantly change the mechanical properties. More dislocations in the lattice results in much lower Young's modulus, bulk and shear moduli. However, Cu substitutional alloying in m6 may suppress the dislocation formation, resulting in higher elastic properties than m5.

In PbSe-based HE models, both strains and Grüneisen parameter have been increased through alloying by increasing x content of $Pb_{0.99-y}Sb_{0.012}Sn_ySe_{1-2x}Te_xS_x$. Rafal et al.[116] has shown that enhancing bond anharmonicity by alloying of $Pb_{1-x}Sn_xTe$ results in larger γ_α which in return results in a reduced κ_L. We conclude that alloying with Sb, Sn, Te, and S atoms caused an increase of elastic strains and γ_α, a reduction of phonon velocity, Debye temperature, and consequently a significant reduction in κ_L. There is a dramatic decrease in the values of elastic constants (C_{11}, C_{22}, C_{33}) as x content increases to 0.25 (see Fig. 2a), indicating a significant change in the

deformation resistance of the $Pb_{0.99}Sb_{0.012}Se_{0.5}Te_{0.25}S_{0.25}$ model. This dramatic decrease (at x = 0.25) in the values of elastic constants causes a dramatic decline of v_s, v_m, and θ_D of $Pb_{0.99}Sb_{0.012}Se_{0.5}Te_{0.25}S_{0.25}$ (see Fig. 2c and d). Elastic moduli exhibit a decline as the x content increases, and the identical trend is observed for mechanical properties–Young's, bulk, and shear moduli. However, there is dramatic decrease in mechanical properties at the x content of 0.25 (see Fig.S21a–c). This indicates a dramatic decline of the deformation resistance of this HE solid solution ($Pb_{0.99}Sb_{0.012}Se_{0.5}Te_{0.25}S_{0.25}$). At x = 0.25, κ and κ_L have also the smallest values (see Fig. 3b and c), indicating larger lattice distortion, which can strengthen phonon scattering due to mass and strain field fluctuations in matrix lattice. Lattice distortion introduced by Te and S alloying in PbSe is favorable for dislocation formation. Higher dislocation density indicates very small κ_L. Our calculations show that the denser dislocation may occur at x = 0.25 ($Pb_{0.99}Sb_{0.012}Se_{0.5}Te_{0.25}S_{0.25}$). After x = 0.25, the dislocation density starts decreasing and causing higher κ_L and elastic properties.

Conclusion

The elastic and thermal properties of pure GeTe(m0) and nine high-entropy models: $Ge_{0.77}Ag_{0.11}Pb_{0.12}Te(m1)$, $Ge_{0.75}Sb_{0.13}Pb_{0.12}Te(m2)$, $Ge_{0.74}Ag_{0.11}Sb_{0.13}Te(m3)$, $Ge_{0.62}Ag_{0.11}Sb_{0.13}Pb_{0.12}Te(m4)$, $Ge_{0.61}Ag_{0.11}Sb_{0.13}Pb_{0.12}Bi_{0.01}Te(m5)$, $Ge_{0.61}Ag_{0.11}Sb_{0.13}Pb_{0.12}Bi_{0.01}Cu_{0.003}Te(m6)$, $Ge_{0.61}Ag_{0.11}Sb_{0.13}Pb_{0.12}Cd_{0.05}Bi_{0.01}Te(m7)$, $Ge_{0.61}Ag_{0.11}Sb_{0.13}Pb_{0.12}Mn_{0.05}Bi_{0.01}$ T(m8), and $Ge_{0.61}Ag_{0.11}Sb_{0.13}Pb_{0.12}Sn_{0.05}Bi_{0.01}Te(m9)$ were investigated using first-principles calculations. The alloying of these solid solutions was carried out using the random solid solution model (RSSM) which is efficient for large supercells of 1080 atoms. Based on our calculations, m0 and all nine solid solution models are mechanically stable. m5 has the lowest Young's, bulk and shear moduli. Generally speaking, random alloying of GeTe by Ag, Sb, Pb, Bi, Cu, Mn, Cd, and Sn elements at the Ge sites results in a reduced hardness, sound velocity, Debye temperature, and thermal conductivity. Among the nine solid solution models, m2, m5, m8 have the lowest Debye temperature and thermal conductivity. m1, m2, m5, and m8 have much lower lattice thermal conductivity compared to pure GeTe (m0). The models m2, m5, and m8 have the lowest and comparable values of κ_L (see Fig. 1f). Mechanical and thermal properties of thirteen PbSe-based high-entropy chalcogenide models: $Pb_{0.99-y}Sb_{0.012}Sn_ySe_{1-2x}Te_xS_x$ (x = 0.1, 0.2, 0.25, 0.3, 0.35, 0.4, 0.45, and y = 0) and $Pb_{0.99-y}Sb_{0.012}Sn_ySe_{1-2x}Te_xS_x$ (y = 0.05, 0.1, 0.15, 0.2, 0.25 and x = 0.25) are investigated in detail. The reduction in speed of sound and lattice thermal conductivity correspond to an increase in internal elastic strains. We conclude that alloying with Sb, Sn, Te, and S atoms caused an increase of elastic strains and γ_α, a reduction of phonon velocity, Debye temperature, and consequently a significant reduction in κ_L. Despite a large number of complex calculations on mechanical and thermal properties of very large supercells of high-entropy chalcogenides were done for the first time, there are obviously some drawbacks such as ignoring the lattice dynamics(phonon calculations), However, phonon calculations is almost impossible to be carried out for such large supercells. We are encouraged by the current results and aspire to continue research in this direction for more complex and interesting high-entropy chalcogenides. It is desirable to improve the DFT calculations with better options, such as using either hybrid potential or Becke–Johnson potential. Finally, we believe our results can facilitate the design of new high-entropy chalcogenides with better thermoelectric performance.

Materials and methods
Density functional theory method

Density functional theory (DFT) based method is utilized to perform the calculations implemented in the *Vienna Ab initio Simulation Package* (VASP)[128]. VASP is used to optimize the structures of solid solution models and calculate the mechanical properties. The one-electron orbitals are expanded in the plane wave basis set with an energy cut-off of 600 eV. The generalized gradient approximation (GGA) of Perdew, Burke, and Ernzerhof (PBE)[129] is used as the exchange and correlation potential for solving the Kohn–Sham equation. The electronic and ionic force convergence criteria are set at 10^{-6} eV and 10^{-5} eV/Å respectively. The Monkhorst scheme[130] is used with k-point meshes of $2 \times 2 \times 1$ for GeTe-based HE solid solutions, while k-point meshes of $1 \times 1 \times 1$ were used for all PbSe-based HE solid solutions. The stress vs strain scheme is used to calculate the elastic tensor. The following linear equation, also called the Hooke's law, can be solved to obtain the elastic coefficient, C_{ij}:

$$\sigma_i = \sum_{j=1} C_{ij}\epsilon_j, \tag{6}$$

where i and j range from 1 to 6. The σ_i is obtained by applying a strain ϵ_j of $+0.50\%$ and -0.50% to the equilibrium structure. More details on mechanical properties calculation are described in SI.

Supercell construction

GeTe-based supercells for high-entropy chalcogenide models in trigonal lattice are constructed based on the random solid solution model (RSSM). In RSSM method, the determination of the number of atoms, N, in the supercell is crucial. N in all ten models is calculated by the simple formula: $N = 6 \times (n^2 \times m)$, where the number 6 is the number of atoms in the GeTe simple cell. n and m are set to be 6 and 5, respectively, so N is 1080 atoms in the trigonal supercell. The lengths of the supercells equal to $n \times a$ and $m \times c$, where a and c are the lattice constants of the simple trigonal GeTe crystal. RSSM method requires a large supercell with large number of atoms. A 1080-atom supercell can be considered to be the minimal size to justify the use of RSSM with high confidence. It is necessary to use "supercell" to capture different possible structural configurations of the HE models. In the present study, we assure that the statistical distribution of random distribution of alloying elements (Ag, Sb, Pb, Bi, Cu, Cd, Mn, and Sn) is sufficient due to sufficiently large supercell with periodical boundary conditions that can account for the random distribution of the NN, second NN, and the third NN for each atom in the model.

In compliance with the spirit of RSSM, it is carried out by writing a small script such that the atomic occupation of each site is completely random with no restriction to their NN atoms and beyond[131]. For PbSe-based HE models, the same procedure was followed, except that the formula of N was set to be: $N = 8 \times (n^3)$, where the number 8 is the number of atoms in the PbSe simple cell and n is set to be 5. The lengths of the supercells equal to $n \times a$ where a is the lattice constant of the simple cubic PbSe crystal.

Data availability

References

1. Yeh, J. W. *et al.* Nanostructured high-entropy alloys with multiple principal elements: Novel alloy design concepts and outcomes. *Adv. Eng. Mater.* **6**, 299–303 (2004).
2. Yeh, J. W. Alloy design strategies and future trends in high-entropy alloys. *JOM* **65**, 1759–1771 (2013).
3. Gao, M. C. *et al.* Computational modeling of high-entropy alloys: Structures, thermodynamics and elasticity. *J. Mater. Res.* **32**, 3627–3641 (2017).
4. Yeh, J. W., Chen, Y. L., Lin, S. J. & Chen, S. K. High-entropy alloys—A new era of exploitation. *Mater. Sci. Forum* **560**, 1–9 (2007).
5. Zhu, H. *et al.* Entropy engineered cubic n-type AgBiSe2 alloy with high thermoelectric performance in fully extended operating temperature range. *Adv. Energy Mater.* **11**, 1–9 (2021).
6. Sun, L. & Cava, R. J. High-entropy alloy superconductors: Status, opportunities, and challenges. *Phys. Rev. Mater.* **3**, 1–10 (2019).
7. Tsao, T. K. *et al.* The high temperature tensile and creep behaviors of high entropy superalloy. *Sci. Rep.* **7**, 1–9 (2017).
8. Li, Z., Tasan, C. C., Springer, H., Gault, B. & Raabe, D. Interstitial atoms enable joint twinning and transformation induced plasticity in strong and ductile high-entropy alloys. *Sci. Rep.* **7**, 1–7 (2017).
9. Bérardan, D., Franger, S., Dragoe, D., Meena, A. K. & Dragoe, N. Colossal dielectric constant in high entropy oxides. *Phys. Status Solidi Rapid Res. Lett.* **10**, 328–333 (2016).
10. Stolze, K., Tao, J., Von Rohr, F. O., Kong, T. & Cava, R. J. Sc-Zr-Nb-Rh-Pd and Sc-Zr-Nb-Ta-Rh-Pd high-entropy alloy superconductors on a CsCl-type lattice. *Chem. Mater.* **30**, 906–914 (2018).
11. Ye, Y. F., Wang, Q., Lu, J., Liu, C. T. & Yang, Y. High-entropy alloy: Challenges and prospects. *Mater. Today* **19**, 349–362 (2016).
12. Rost, C. M. *et al.* Electron and phonon thermal conductivity in high entropy carbides with variable carbon content. *Acta Mater.* **196**, 231–239 (2020).
13. Juan, C. C. *et al.* On microstructure and mechanical performance of AlCoCrFeMo 0.5Ni x high-entropy alloys. *Intermetallics* **32**, 401–407 (2013).
14. Zou, Y., Ma, H. & Spolenak, R. Ultrastrong ductile and stable high-entropy alloys at small scales. *Nat. Commun.* https://doi.org/10.1038/ncomms8748 (2015).
15. Hsu, C.-Y., Yeh, J.-W., Chen, S.-K. & Shun, T.-T. Wear resistance and high-temperature compression strength of Fcc CuCoNiCrAl. *Metall. Mater. Trans. A Phys. Metall. Mater. Sci.* **35**, 1465–1469 (2004).
16. Chou, Y. L., Wang, Y. C., Yeh, J. W. & Shih, H. C. Pitting corrosion of the high-entropy alloy Co1.5CrFeNi1.5Ti0.5Mo0.1 in chloride-containing sulphate solutions. *Corros. Sci.* **52**, 3481–3491 (2010).
17. Sharma, Y. *et al.* Single-crystal high entropy perovskite oxide epitaxial films. *Phys. Rev. Mater.* **2**, 1–6 (2018).
18. Jiang, S. *et al.* A new class of high-entropy perovskite oxides. *Scr. Mater.* **142**, 116–120 (2018).
19. Gild, J. *et al.* High-entropy metal diborides: A new class of high-entropy materials and a new type of ultrahigh temperature ceramics. *Sci. Rep.* **6**, 2–11 (2016).
20. Castle, E., Csanádi, T., Grasso, S., Dusza, J. & Reece, M. Processing and properties of high-entropy ultra-high temperature carbides. *Sci. Rep.* **8**, 1–12 (2018).
21. Sarker, P. *et al.* High-entropy high-hardness metal carbides discovered by entropy descriptors. *Nat. Commun.* **9**, 1–10 (2018).
22. Desai, S. B. *et al.* Supplementary materials for MoS 2 transistors with 1-nanometer gate lengths. *Science* **354**, 99–103 (2016).
23. Wang, W. *et al.* Device characteristics of CZTSSe thin-film solar cells with 12.6% efficiency. *Adv. Energy Mater.* **4**, 1–5 (2014).
24. Yang, P. Semiconductor nanowires for energy conversion. *ACS Natl. Meet. B Abstr.* https://doi.org/10.1109/inec.2010.5424441 (2010).
25. Williams, L. & Kioupakis, E. BInGaN alloys nearly lattice-matched to GaN for high-power high-efficiency visible LEDs. *Appl. Phys. Lett.* **111**, 1–6 (2017).
26. Peidong Yang, C. Z. N., Dou, L. & Yang, P. Bandgap engineering in semiconductor alloy nanomaterials with widely tunable compositions. *Nat. Rev. Mater.* https://doi.org/10.1038/natrevmats.2017.70 (2017).
27. Sau, J. D. & Cohen, M. L. Possibility of increased mobility in Ge-Sn alloy system. *Phys. Rev. B Condens. Matter Mater. Phys.* **75**, 1–7 (2007).
28. Qin, B. *et al.* Comprehensive investigation on the thermoelectric properties of p-type PbTe-PbSe-PbS alloys. *Adv. Electron. Mater.* **5**, 1–8 (2019).
29. Qiu, Y. *et al.* Realizing high thermoelectric performance in GeTe through decreasing the phase transition temperature: Via entropy engineering. *J. Mater. Chem. A* **7**, 26393–26401 (2019).
30. Hien, N. D. *et al.* First principles study of single-layer SnSe 2 under biaxial strain and electric field: Modulation of electronic properties. *Phys. E Low Dimens. Syst. Nanostruct.* **111**, 201–205 (2019).
31. Guo, R., Wang, X., Kuang, Y. & Huang, B. First-principles study of anisotropic thermoelectric transport properties of IV-VI semiconductor compounds SnSe and SnS. *Phys. Rev. B Condens. Matter Mater. Phys.* **92**, 1–13 (2015).
32. Liu, M. *et al.* The crystallization, thermodynamic and thermoelectric properties of vast off-stoichiometric Sn-Se crystals. *J. Mater. Chem. C* **8**, 6422–6434 (2020).
33. Tan, X. *et al.* Optimizing the thermoelectric performance of In-Cd codoped SnTe by introducing Sn vacancies. *J. Mater. Chem. C* **5**, 7504–7509 (2017).
34. Yuan, K., Sun, Z., Zhang, X., Gong, X. & Tang, D. A first-principles study of the thermoelectric properties of rhombohedral GeSe. *Phys. Chem. Chem. Phys.* **22**, 1911–1922 (2020).
35. Nam, K. H. *et al.* New high-energy-density GeTe-based anodes for Li-ion batteries. *J. Mater. Chem. A* **7**, 3278–3288 (2019).
36. Hu, L., Huang, S., Patterson, R. & Halpert, J. E. Enhanced mobility in PbS quantum dot films: Via PbSe quantum dot mixing for optoelectronic applications. *J. Mater. Chem. C* **7**, 4497–4502 (2019).
37. Roy, P. & Nguyen, T. P. Ab initio calculation of pentacene-PbSe hybrid interface for photovoltaic applications. *Phys. Chem. Chem. Phys.* **18**, 18209–18218 (2016).

13

38. Bafekry, A., Stampfl, C. & Peeters, F. M. The electronic, optical, and thermoelectric properties of monolayer PbTe and the tunability of the electronic structure by external fields and defects. *Phys. Status Solidi Basic Res.* **257**, 1–12 (2020).
39. He, J. & Tritt, T. M. Advances in thermoelectric materials research: Looking back and moving forward. *Science* https://doi.org/10.1126/science.aak9997 (2017).
40. Yan, X. *et al.* Experimental studies on anisotropic thermoelectric properties and structures of n-type Bi2Te2.7Se0.3. *Nano Lett.* **10**, 3373–3378 (2010).
41. Hong, M. *et al.* N-type Bi2Te3-xSex nanoplates with enhanced thermoelectric efficiency driven by wide-frequency phonon scatterings and synergistic carrier scatterings. *ACS Nano* **10**, 4719–4727 (2016).
42. Wenke, H. High thermoelectric performance in low-cost SnS0.91Se0.09 crystals. *Science* **365**, 1418–1424 (2019).
43. Samanta, M. & Biswas, K. Low thermal conductivity and high thermoelectric performance in (GeTe)1−2x(GeSe)x(GeS)x: Competition between solid solution and phase separation. *J. Am. Chem. Soc.* **139**, 9382–9391 (2017).
44. Dong, J. *et al.* Medium-temperature thermoelectric GeTe: Vacancy suppression and band structure engineering leading to high performance. *Energy Environ. Sci.* **12**, 1396–1403 (2019).
45. Liu, R. *et al.* Entropy as a gene-like performance indicator promoting thermoelectric materials. *Adv. Mater.* **29**, 1–7 (2017).
46. Fan, Z., Wang, H., Wu, Y., Liu, X. & Lu, Z. Thermoelectric performance of PbSnTeSe high-entropy alloys. *Mater. Res. Lett.* **5**, 187–194 (2017).
47. Hu, L. *et al.* Entropy engineering of SnTe: Multi-principal-element alloying leading to ultralow lattice thermal conductivity and state-of-the-art thermoelectric performance. *Adv. Energy Mater.* **8**, 1–14 (2018).
48. Luo, Y. *et al.* High thermoelectric performance in the new cubic semiconductor AgSnSbSe3by high-entropy engineering. *J. Am. Chem. Soc.* **142**, 15187–15198 (2020).
49. Amiri, A. & Shahbazian-Yassar, R. Recent progress of high-entropy materials for energy storage and conversion. *J. Mater. Chem. A* **9**, 782–823 (2021).
50. Pickering, E. J. & Jones, N. G. High-entropy alloys: A critical assessment of their founding principles and future prospects. *Int. Mater. Rev.* **61**, 183–202 (2016).
51. Gao, M. C. *et al.* High-entropy functional materials. *J. Mater. Res.* **33**, 3138–3155 (2018).
52. Raphel, A., Vivekanandhan, P. & Kumaran, S. High entropy phenomena induced low thermal conductivity in BiSbTe1.5Se1.5 thermoelectric alloy through mechanical alloying and spark plasma sintering. *Mater. Lett.* **269**, 127672 (2020).
53. Korkosz, R. J. *et al.* High ZT in p-type (PbTe)1−2x(PbSe)x(PbS)x thermoelectric materials. *J. Am. Chem. Soc.* **136**, 3225–3227 (2014).
54. Li, J., Zhang, X., Lin, S., Chen, Z. & Pei, Y. Realizing the high thermoelectric performance of GeTe by Sb-doping and Se-alloying. *Chem. Mater.* **29**, 605–611 (2017).
55. Li, J. *et al.* Low-symmetry rhombohedral GeTe thermoelectrics. *Joule* **2**, 976–987 (2018).
56. Xia, Y. & Chan, M. K. Y. Anharmonic stabilization and lattice heat transport in rocksalt β -GeTe. *Appl. Phys. Lett.* https://doi.org/10.1063/1.5048814 (2018).
57. Zheng, Z. *et al.* Rhombohedral to cubic conversion of GeTe via MnTe alloying leads to ultralow thermal conductivity, electronic band convergence, and high thermoelectric performance. *J. Am. Chem. Soc.* **140**, 2673–2686 (2018).
58. Perumal, S., Roychowdhury, S. & Biswas, K. High performance thermoelectric materials and devices based on GeTe. *J. Mater. Chem. C* **4**, 7520–7536 (2016).
59. Shaltaf, R., Durgun, E. & Gonze, X. Dynamical, dielectric, and elastic properties of GeTe investigated with first-principles density functional theory. *Phys. Rev. B* **78**, 1–7. https://doi.org/10.1103/PhysRevB.78.205203 (2008).
60. Perumal, S., Roychowdhury, S., Negi, D. S., Datta, R. & Biswas, K. High thermoelectric performance and enhanced mechanical stability of p-type Ge1-xSbxTe. *Chem. Mater.* **27**, 7171–7178 (2015).
61. Wu, D. *et al.* Origin of the high performance in GeTe-based thermoelectric materials upon Bi2Te3 doping. *J. Am. Chem. Soc.* **136**, 11412–11419 (2014).
62. Hong, M. *et al.* Realizing zT of 2.3 in Ge1−x−ySbxInyTe via reducing the phase-transition temperature and introducing resonant energy doping. *Adv. Mater.* **30**, 1–8 (2018).
63. Hong, M. *et al.* Strong phonon-phonon interactions securing extraordinary thermoelectric Ge1- xSbxTe with Zn-alloying-induced band alignment. *J. Am. Chem. Soc.* **141**, 1742–1748 (2019).
64. Hong, M. *et al.* Arrays of planar vacancies in superior thermoelectric Ge1−x−yCdxBiyTe with band convergence. *Adv. Energy Mater.* **8**, 1–10 (2018).
65. Liu, Z. *et al.* Phase-transition temperature suppression to achieve cubic GeTe and high thermoelectric performance by Bi and Mn codoping. *Proc. Natl. Acad. Sci. U.S.A.* **115**, 5332–5337 (2018).
66. Jiang, B. *et al.* High figure-of-merit and power generation in high-entropy GeTe-based thermoelectrics. *Science* **213**, 208–213 (2022).
67. Heremans, J. P. *et al.* Enhancement of thermoelectric of the electronic density of states. *Science* **321**, 1457–1461 (2008).
68. Wang, H., Pei, Y., Lalonde, A. D. & Snyder, G. J. Heavily doped p-type PbSe with high thermoelectric performance: An alternative for PbTe. *Adv. Mater.* **23**, 1366–1370 (2011).
69. Wang, H., Schechtel, E., Pei, Y. & Snyder, G. J. High thermoelectric efficiency of n-type PbS. *Adv. Energy Mater.* **3**, 488–495 (2013).
70. Dalven, R. Electronic structure of PbS, PbSe, and PbTe. *Solid State Phys. Adv. Res. Appl.* **28**, 179–224 (1974).
71. Zhang, Y., Ke, X., Chen, C., Yang, J. & Kent, P. R. C. Thermodynamic properties of PbTe, PbSe, and PbS: First-principles study. *Phys. Rev. B Condens. Matter Mater. Phys.* **80**, 1–12 (2009).
72. Zhang, Q. *et al.* Study of the thermoelectric properties of lead selenide doped with Boron, gallium, indium, or thallium. *J. Am. Chem. Soc.* **134**, 17731–17738 (2012).
73. Androulakis, J., Lee, Y., Todorov, I., Chung, D. Y. & Kanatzidis, M. High-temperature thermoelectric properties of n-type PbSe doped with Ga, In, and Pb. *Phys. Rev. B Condens. Matter Mater. Phys.* **83**, 1–9 (2011).
74. Zhang, Q. *et al.* Enhancement of thermoelectric figure-of-merit by resonant states of aluminium doping in lead selenide. *Energy Environ. Sci.* **5**, 5246–5251 (2012).
75. Chen, Z. *et al.* Vacancy-induced dislocations within grains for high-performance PbSe thermoelectrics. *Nat. Commun.* **8**, 1–8 (2017).
76. Nemov, S. A., Gavrikova, T. A., Zykov, V. A., Osipov, P. A. & Proshin, V. I. Features of the electrical compensation of bismuth impurities in PbSe. *Semiconductors* **32**, 689–691 (1998).
77. Jiang, B. *et al.* High-entropy-stabilized chalcogenides with high thermoelectric performance. *Science* **371**, 830–834 (2021).
78. Jiang, B. *et al.* Entropy engineering promotes thermoelectric performance in p-type chalcogenides. *Nat. Commun.* **12**, 1–8 (2021).
79. Peng, K. *et al.* Ultra-high average figure of merit in synergistic band engineered Sn x Na 1 À x Se 0.9S0.1 single crystals. *Mater. Today* **21**, 1–7 (2017).
80. Zhao, Q. *et al.* Synergistically optimized electrical and thermal transport properties of polycrystalline SnSe via alloying SnS. *J. Solid State Chem.* https://doi.org/10.1016/j.jssc.2019.02.038 (2019).
81. Joshi, G. *et al.* Enhanced thermoelectric figure-of-merit in nanostructured p-type silicon germanium bulk alloys. *Nano Lett.* **8**, 4670–4674. https://doi.org/10.1021/nl8026795 (2008).

82. Morelli, D. T. & Jovovic, V. Intrinsically minimal thermal conductivity in cubic I - V - VI 2 semiconductors. *Phys. Rev. Lett.* **035901**, 16–19 (2008).

83. Chen, Z. *et al.* Lattice dislocations enhancing thermoelectric pbte in addition to band convergence. *Adv. Mater.* **1606768**, 1–8 (2017).

84. Wu, Y. *et al.* Lattice strain advances thermoelectrics lattice strain advances thermoelectrics. *Joule* **3**, 1–13. https://doi.org/10.1016/j.joule.2019.02.008 (2019).

85. Zunger, A. Special quasirandom structures. *Phys. Rev. Lett.* **65**, 353–356 (1990).

86. King, D. J. M., Burr, P. A., Obbard, E. G. & Middleburgh, S. C. DFT study of the hexagonal high-entropy alloy fission product system. *J. Nucl. Mater.* **488**, 70–74 (2017).

87. Mouhat, F. & Coudert, F. X. Necessary and sufficient elastic stability conditions in various crystal systems. *Phys. Rev. B Condens. Matter Mater. Phys.* **90**, 0–3 (2014).

88. Deng, H. Theoretical prediction of the structural, electronic, mechanical and thermodynamic properties of the binary α-As$_2$Te$_3$ and β-As$_2$Te$_3$. *J. Alloys Compd.* **656**, 695–701 (2015).

89. Kleinman, L. Deformation potentials in silicon. *Phys. Rev.* **128**, 2614 (1962).

90. Hill, R. The elastic behaviour of a crystalline aggregate. *Proc. Phys. Soc. Sect. A* **65**, 349–354 (1952).

91. Pugh, S. F. Relations between the elastic moduli and the plastic properties of polycrystalline pure metals. *Philos. Mag. Ser. 7* **45**(367), 823–843 (1954).

92. Phasha, M. J., Ngoepe, P. E., Chauke, H. R., Pettifor, D. G. & Nguyen-Mann, D. Link between structural and mechanical stability of fcc- And bcc-based ordered Mg-Li alloys. *Intermetallics* **18**, 2083–2089 (2010).

93. Ali, M. *et al.* First-principles study of elastic, electronic, optical and thermoelectric properties of newly synthesized K$_2$Cu$_2$GeS$_4$ chalcogenide. *J. Alloys Compd.* **781**, 37–46 (2019).

94. Heciri, D. *et al.* Insight into the structural, elastic and electronic properties of tetragonal inter-alkali metal chalcogenides CsNaX (X=S, Se, and Te) from first-principles calculations. *Mater. Chem. Phys.* **221**, 125–137 (2019).

95. Thakur, V. & Pagare, G. Theoretical calculations of elastic, mechanical and thermal properties of REPt3 (RE = Sc, Y and Lu) intermetallic compounds based on DFT. *Indian J. Phys.* **92**, 1503–1513 (2018).

96. Chen, X. Q., Niu, H., Li, D. & Li, Y. Modeling hardness of polycrystalline materials and bulk metallic glasses. *Intermetallics* **19**, 1275–1281 (2011).

97. Tian, Y., Xu, B. & Zhao, Z. Microscopic theory of hardness and design of novel superhard crystals. *Int. J. Refract. Met. Hard. Mater.* **33**, 93–106 (2012).

98. Liu, Z. T. Y., Zhou, X., Gall, D. & Khare, S. V. First-principles investigation of the structural, mechanical and electronic properties of the NbO-structured 3d, 4d and 5d transition metal nitrides. *Comput. Mater. Sci.* **84**, 365–373 (2014).

99. Liu, Z. T. Y., Zhou, X., Khare, S. V. & Gall, D. Structural, mechanical and electronic properties of 3d transition metal nitrides in cubic zincblende, rocksalt and cesium chloride structures: A first-principles investigation. *J. Phys. Condens. Matter* **26**, 025404 (2014).

100. Zhou, X., Gall, D. & Khare, S. V. Mechanical properties and electronic structure of anti-ReO$_3$ structured cubic nitrides, M3N, of d block transition metals M: An ab initio study. *J. Alloys Compd.* **595**, 80–86 (2014).

101. Luan, X. *et al.* The mechanical properties and elastic anisotropies of cubic Ni$_3$Al from first principles calculations. *Crystals* **8**, 307 (2018).

102. Strnad, G. & Jakab-Farkas, L. Improving the accuracy of low-load vickers microhardness testing of hard thin films. *Procedia Technol.* **12**, 289–294 (2014).

103. Caravaca, M. A. *et al.* Model for Vickers microhardness prediction applied to SnO$_2$ and TiO$_2$ in the normal and high pressure phases. *J. Eur. Ceram. Soc.* **34**, 3791–3800 (2014).

104. Bao, L., Qu, D., Kong, Z. & Duan, Y. Anisotropies in elastic properties and thermal conductivities of trigonal TM2C (TM = V, Nb, Ta) carbides. *Solid State Sci.* **98**, 106027 (2019).

105. Hossain, M. M. *et al.* Influence of Se doping on recently synthesized NaInS2-xSex solid solutions for potential thermo-mechanical applications studied via first-principles method. *Mater. Today Commun.* **26**, 101988 (2021).

106. Surucu, G., Isik, M., Candan, A., Wang, X. & Gullu, H. H. Investigation of structural, electronic, magnetic and lattice dynamical properties for XCoBi (X: Ti, Zr, Hf) Half-Heusler compounds. *Phys. B Condens. Matter* **587**, 412146 (2020).

107. Sun, L., Gao, Y., Xiao, B., Li, Y. & Wang, G. Anisotropic elastic and thermal properties of titanium borides by first-principles calculations. *J. Alloys Compd.* **579**, 457–467 (2013).

108. Gaillac, R., Pullumbi, P. & Coudert, F. X. ELATE: An open-source online application for analysis and visualization of elastic tensors. *J. Phys. Condens. Matter* **28**, 275201 (2016).

109. Yang, A., Bao, L., Peng, M. & Duan, Y. Explorations of elastic anisotropies and thermal properties of the hexagonal TMSi2 (TM = Cr, Mo, W) silicides from first-principles calculations. *Mater. Today Commun.* **27**, 102474 (2021).

110. Ma, H., Zhang, X. & Wang, F. First-principles study of the lattice vibration, elastic anisotropy and thermodynamical properties of Tantalum Silicide with the different crystal structures. *Vacuum* **191**, 110410 (2021).

111. Li, X. Y. *et al.* Observation of high-frequency transverse phonons in metallic glasses. *Phys. Rev. Lett.* **124**, 1–6 (2020).

112. Shen, Y., Clarke, D. R. & Fuierer, P. A. Anisotropic thermal conductivity of the Aurivillus phase, bismuth titanate (Bi4Ti3O12): A natural nanostructured superlattice. *Appl. Phys. Lett.* **93**, 1–4 (2008).

113. Clarke, D. R. Materials selections guidelines for low thermal conductivity thermal barrier coatings. *Surf. Coat. Technol.* **163–164**, 67–74 (2003).

114. Cahill, D. G., Watson, S. K. & Pohl, R. O. Lower limit to the thermal conductivity of disordered crystals. *Phys. Rev. B* **46**, 6131–6140 (1992).

115. Morelli, D. T. & Slack, G. A. High lattice thermal conductivity solids. *High Therm. Conduct. Mater.* https://doi.org/10.1007/0-387-25100-6_2 (2006).

116. Knura, R. & Parashchuk, T. Origins of low lattice thermal conductivity of Pb 1−x Sn x Te alloys for thermoelectric applications. *Dalton Trans.* https://doi.org/10.1039/d0dt04206d (2021).

117. Bhowmick, S. Effect of strain on the thermal conductivity of solids. *J. Chem. Phys.* https://doi.org/10.1063/1.2361287 (2006).

118. Feng, J. *et al.* Electronic structure, mechanical properties and thermal conductivity of Ln2Zr2O7 (Ln = La, Pr, Nd, Sm, Eu and Gd) pyrochlore. *Acta Mater.* **59**, 1742–1760 (2011).

119. Malhotra, A. & Maldovan, M. Impact of phonon surface scattering on thermal energy distribution of Si and SiGe nanowires. *Nat. Publ. Gr.* **6**, 1–13. https://doi.org/10.1038/srep25818 (2016).

120. Murphy, K. F. Scholarly commons strain effects on thermal conductivity of nanostructured silicon by raman piezothermography strain effects on thermal conductivity of nanostructured silicon by Raman (2014).

121. Yang, Y., Wang, W., Gan, G.-Y. & Xue-Feng Shi, B.-Y.T. Structural, mechanical and electronic properties of (TaNbHfTiZr)C high entropy carbide under pressure: Ab initio investigation. *Phys. B Phys. Condens. Matter* **550**, 163–170 (2018).

122. Zhao, L. D. *et al.* Ultralow thermal conductivity and high thermoelectric figure of merit in SnSe crystals. *Nature* **508**, 373–377 (2014).

123. Zeier, W. G. *et al.* Thinking like a chemist: Intuition in thermoelectric materials. *Angew. Chem. Int. Ed.* https://doi.org/10.1002/anie.201508381 (2016).

124. Jia, T., Chen, G. & Zhang, Y. Lattice thermal conductivity evaluated using elastic properties. *Phys. Rev. B* https://doi.org/10.1103/PhysRevB.95.155206 (2017).
125. Hanus, R. *et al.* Lattice softening significantly reduces thermal conductivity and leads to high thermoelectric efficiency. *Adv. Mater.* **31**, 1900108. https://doi.org/10.1002/adma.201900108 (2019).
126. Brugger, K. Generalized Griineisen parameters in the anisotropic Debye model. *Phys. Rev.* https://doi.org/10.1103/PhysRev.137.A1826 (1965).
127. Xu, L. *et al.* Dense dislocations enable high-performance PbSe thermoelectric at low-medium temperatures. *Nat. Commun.* **13**, 6449. https://doi.org/10.1038/s41467-022-34227-3 (2022).
128. Kresse, G. Efficient iterative schemes for ab initio total-energy calculations using a plane-wave basis set. *Phys. Rev. B* **54**, 11169–11186 (1996).
129. Perdew, J. P., Burke, K. & Ernzerhof, M. Generalized gradient approximation made simple. *Phys. Rev. Lett.* **77**, 3865–3868 (1996).
130. Monkhorst, H. J. & Pack, J. D. Special points for Brillonin-zone integrations*. *Phys. Rev. B* **13**, 5188–5192 (1976).
131. Ching, W. & Liaw, P. K. Fundamental electronic structure and multiatomic bonding in 13 biocompatible high-entropy alloys. *NPJ Comput. Mater.* https://doi.org/10.1038/s41524-020-0321-x (2020).

Acknowledgements

Author contributions

W.C. conceived and directed the project. W.C. and S.H. performed the calculations. S.H. and P.A. made all figures. S.H., P.A., S.S., and W.C. drafted the paper. All authors participated in the discussion and interpretation of the results. All authors edited and proofread the final manuscript.

Competing interests

The authors declare no competing interests.

Additional information

Supplementary Information The online version contains supplementary material available at https://doi.org/10.1038/s41598-023-42101-5.

Correspondence and requests for materials should be addressed to W.-Y.C.

Reprints and permissions information is available at www.nature.com/reprints.

Publisher's note Springer Nature remains neutral with regard to jurisdictional claims in published maps and institutional affiliations.